Temperature dependence of magnetic anisotropy and magnetoelasticity from classical spin-lattice calculations

S. Nikolov [1,*] P. Nieves [2] A. P. Thompson,[1] M. A. Wood,[1] and J. Tranchida[3]

[1]*Computational Multiscale Department, Sandia National Laboratories, P.O. Box 5800, Albuquerque, New Mexico 87185, USA*

[2]*IT4Innovations, VŠB - Technical University of Ostrava, 17 listopadu 2172/15, 70800 Ostrava-Poruba, Czech Republic*

[3]*CEA, DES, IRESNE, DEC, SESC, LM2C, F-13108 Saint-Paul-Lez-Durance, France*

(Received 30 November 2022; revised 24 February 2023; accepted 1 March 2023; published 23 March 2023)

We present a classical molecular-spin dynamics (MSD) methodology that enables accurate computations of the temperature dependence of the magnetocrystalline anisotropy as well as magnetoelastic properties of magnetic materials. The nonmagnetic interactions are accounted for by a spectral neighbor analysis potential (SNAP) machine-learned interatomic potential, whereas the magnetoelastic contributions are accounted for using a combination of an extended Heisenberg Hamiltonian and a Néel pair interaction model, representing both the exchange interaction and spin-orbit-coupling effects, respectively. All magnetoelastic potential components are parameterized using a combination of first-principles and experimental data. Our framework is applied to the α phase of iron. Initial testing of our MSD model is done using a 0 K parametrization of the Néel interaction model. After this, we examine how individual Néel parameters impact the B_1 and B_2 magnetostrictive coefficients using a moment-independent δ sensitivity analysis. The results from this study are then used to initialize a genetic algorithm optimization which explores the Néel parameter phase space and tries to minimize the error in the B_1 and B_2 magnetostrictive coefficients in the range of 0–1200 K. Our results show that while both the 0 K and genetic algorithm optimized parametrization provide good experimental agreement for B_1 and B_2, only the genetic algorithm optimized results can capture the second peak in the B_1 magnetostrictive coefficient which occurs near approximately 800 K.

DOI: 10.1103/PhysRevB.107.094426

I. INTRODUCTION

Building accurate magnetoelastic material models requires a two-way coupling between lattice deformations and the orientation of the atomic magnetic moment vector [1], for example, a change of sample shape under a magnetic field [2,3] or a magnetization reorientation following an applied strain [4]. Applications leveraging magnetoelastic and magnetostrictive effects are very diverse, from microactuators and sonar transducers to smart components [2,5,6] and spintronics [7–10]. Recent studies successfully investigated the possibility of coupling piezoelectric thin layers to single domain magnetoelastic elements to efficiently shift the magnetization orientation [11]. Such designs could lead to magnetoelectric memory systems with very low energy consumption [12]. The development of scalable numerical tools that enable the construction of accurate material models for such applications at the atomic scale is thus highly desirable.

Coupling lattice deformations and magnetic moment orientations in frameworks such as classical spin-lattice dynamics [13] is also of theoretical interest. It allows one to represent effects arising from orbital magnetism and to perform a direct coupling between lattice and classical spins [14]. In their recent work, Ebert *et al.* illustrated how spin-lattice exchange coupling tensors can be constructed from first-principles calculations and highlighted their potential use for coupled molecular-spin dynamics (MSD) simulations [15,16]. Such approaches are an improvement over the extended Heisenberg Hamiltonians or classical definitions of magnetic anisotropies. Alternate improvements over the extended Heisenberg Hamiltonian have included the addition of biquadratic exchange interactions, which have shown to be relevant for three-dimensional (3D) transition ferromagnets [17,18]. Using an inelastic neutron scattering technique, Strässle *et al.* illustrated that for $CsMn_{0.28}Mg_{0.72}Br_3$, the biquadratic exchange interactions arise from the mechanism of exchange striction [19]. More recently, Zivieri proved that for 1D and 2D ferromagnetic systems, the biquadratic exchange coupling leads to the absence of long-range order at finite temperatures [20].

Within the framework of the classical spin-lattice methodology, Perera *et al.* [21] and Strungaru *et al.* [22] also recently discussed the importance of angular momentum transfer between lattice and magnetic energy reservoirs. Following the work of Beaujouan *et al.* [14], they displayed that empirical models, such as the Néel interaction, can represent those effects. More recently, Nieves *et al.* showed that the Néel interaction can be parametrized to represent zero-temperature magnetocrystalline anisotropy and anisotropic magnetostriction in cubic crystals [23]. Recent first-principles studies leveraged density functional theory (DFT) accounting for the spin-orbit coupling to compute such quantities [24,25]. For spin dynamics (frozen lattice), Asselin *et al.* showed that the constrained Monte Carlo method can accurately and

*Corresponding author: snikolo@sandia.gov

efficiently extract the temperature dependence of magnetic anisotropy [26]. However, to the knowledge of the authors, there is no classical atomistic methodology (incorporating both spin and lattice fluctuations) capable of computing the temperature dependence of the magnetoelastic and magnetostrictive coefficients, as well as the magnetocrystalline anisotropy coefficients.

When a magnetic cubic crystal is strained, its energy can be decomposed into two components. The first one is a purely elastic (magnetization-independent) contribution,

$$E_{el} = \tfrac{1}{2}c_{11}\left(\epsilon_{xx}^2 + \epsilon_{yy}^2 + \epsilon_{zz}^2\right) + \tfrac{1}{2}c_{44}\left(\epsilon_{xy}^2 + \epsilon_{yz}^2 + \epsilon_{zx}^2\right) + c_{12}(\epsilon_{xx}\epsilon_{yy} + \epsilon_{yy}\epsilon_{zz} + \epsilon_{xx}\epsilon_{zz}), \quad (1)$$

with ϵ_{ij} the components of the strain tensor and c_{ij} the elastic constants, and the second one is a magnetoelastic contribution,

$$E_{me} = B_0(\epsilon_{xx} + \epsilon_{yy} + \epsilon_{zz}) + B_1\left(\alpha_x^2\epsilon_{xx} + \alpha_y^2\epsilon_{yy} + \alpha_z^2\epsilon_{zz}\right) + B_2(\alpha_x\alpha_y\epsilon_{xy} + \alpha_y\alpha_z\epsilon_{yz} + \alpha_x\alpha_z\epsilon_{xz}), \quad (2)$$

which couples the strain tensor components with the the magnetization orientations α_i, given by $\alpha_x = \sin(\theta)\cos(\phi)$, $\alpha_y = \sin(\theta)\sin(\phi)$, $\alpha_z = \cos(\theta)$, where ϕ lays in the $x-y$ plane and is measured with respect to the x axis. B_0 is related to the volume magnetoelasticity [27] and does not depends on the magnetization direction.

In this study, we focus on the five remaining coefficients (c_{11}, c_{12}, c_{44}, B_1, and B_2) and the magnetocrystalline anisotropy. While c_{11}, c_{12}, c_{44} are largely determined by the interatomic spectral neighbor analysis potential (SNAP) potential, B_1, B_2, and the magnetocrystalline anisotropy are set by the Néel interaction coefficients. Initially, we parametrize the Néel interaction coefficients to reproduce the zero-temperature magnetocrystalline anisotropy, which is done using the method described in Ref. [23]. The corresponding magnetocrystalline energy surfaces and associated changes with strain at 0 K are examined. Using the zero-temperature Néel parametrization, we then gauge how the magnetoelastic response changes up to 1200 K. After this, we deploy a global sensitivity analysis in order to gauge how different Néel interaction parameters impact the expected values of B_1 and B_2 at different temperatures. The results from this study are used to initialize a genetic algorithm which attempts to minimize the errors in B_1 and B_2 in the range of 0–1200 K (α phase of iron). Our findings show that within a single framework that leverages classical spin-lattice dynamics and an interatomic potential accounting for magnetoelastic effects, the temperature dependence of B_1 and B_2 can be reproduced relatively well. Using both elastic coefficients, we then also compute the temperature dependence of the two magnetostriction coefficients (λ_{100} and λ_{111}). In the first section, we present the methodology used in this work and describe the magnetoelastic interatomic potential generated by combining a machine-learned SNAP potential with a spin Hamiltonian. Additional details regarding magnetoelastic calculations and sensitivity analysis are also provided within the Supplemental Material [28].

II. METHODS

All calculations are performed leveraging the SPIN package of LAMMPS [29,30] and following the classical spin-lattice dynamics approach, as described in Ma *et al.* [13]. The interactions between the atoms and the spins are accounted for through the following spin-lattice Hamiltonian:

$$\mathcal{H}_{sl}(\boldsymbol{r}, \boldsymbol{p}, \boldsymbol{s}) = \sum_{i=1}^{N} \frac{|\boldsymbol{p}_i|^2}{2m_i} + \sum_{i,j=1}^{N} \mathcal{V}^{\mathrm{SNAP}}(r_{ij}) + \mathcal{H}_{\mathrm{ex}}(\boldsymbol{r}, \boldsymbol{s}) + \mathcal{H}_{\mathrm{Néel}}(\boldsymbol{r}, \boldsymbol{s}), \quad (3)$$

where $\boldsymbol{r}_i$, $\boldsymbol{p}_i$, $\boldsymbol{s}_i$, and m_i stand for the position, momentum, normalized magnetic moment, and mass for each atom i in the system, respectively. The first term in the right-hand side of Eq. (3) is the kinetic energy of the atoms. The second one is a machine-learned SNAP interatomic potential representing the purely mechanical interactions in the system [31], whereas the magnetoelastic interactions are accounted for through the combination of the exchange interaction $\mathcal{H}_{\mathrm{ex}}(\boldsymbol{r}, \boldsymbol{s})$ and a Néel pair model $\mathcal{H}_{Néel}(\boldsymbol{r}, \boldsymbol{s})$. The exchange interaction $\mathcal{H}_{\mathrm{ex}}(\boldsymbol{r}, \boldsymbol{s})$ is described by an extended Heisenberg Hamiltonian parameterized from first-principles spin-spiral calculations [32–34]. The Néel pair model used in this work follows the approach described in Nieves *et al.* [23]. Additional information for these two pair styles is provided in Appendix A.

The SNAP potential was trained on a database of first-principles configurations (generated leveraging density functional theory as implemented in the VASP package [35]). The first-principles training set is described in the Methods section of Nikolov *et al.* [34]. This dataset consists of spin-polarized noncollinear VASP calculations for bcc, hcp, and liquid iron. These calculations were performed in the range of <20 GPa and <2000 K. To parametrize the extended Heisenberg Hamiltonian (exchange interactions), we rely on spin-spiral data gathered at different degrees of lattice compression [34]. The exchange interaction fitting is done after the Néel contributions to the forces/energies/stresses have been subtracted out from the DFT spin-spiral training data. After this, the Néel and spin-exchange contributions to the forces/energies/stresses are subtracted out from the remaining DFT training data, leaving only the nonmagnetic potential energy surface. This nonmagnetic potential energy surface is then fitted using a SNAP machine-learned interatomic potential. The training/fitting was performed leveraging the genetic algorithm of the DAKOTA optimization package [36], and results were converged until the mean-absolute error dropped below 100 meV/atom. To obtain good agreement with the c_{11}, c_{12}, and c_{44} elastic constants at temperatures above 0 K, finite-temperature objective functions were integrated into the DAKOTA training procedure. Additional details regarding the SNAP/DAKOTA implementation are provided in Appendix B.

For all MSD calculations, we use 16 000 atom cells ($20 \times 20 \times 20$ bcc cells). Before carrying out any measurements, we initially equilibrate each cell for 50 ps (0.1 fs time step) using the pressure-controlled and magnetization-controlled conditions (PCMCC) scheme, which allows us to relax the pressure and control the magnetization of the system, as detailed in Nikolov *et al.* [34]. To control the magnetization, we follow the approach developed by Evans *et al.* [37], where

we introduce a rescaling between spin and lattice temperatures. The functional form of this rescaling is detailed in Eqs. (4) and (5) below,

$$T_s(T_l) = f_{sw}(T_l - 471.6) + 576 f_{sw}(T_l/1045)^{2.73}, \tag{4}$$

$$f_{sw} = \tfrac{1}{2}\{1 + \tanh[10(T_l - 1045)]\}. \tag{5}$$

Here, T_s and T_l are the spin and lattice thermostat temperatures and f_{sw} is a switching function which ensures that the spin temperature changes smoothly at the Curie temperature. Additional details regarding this temperature rescaling implementation into our molecular-spin dynamics framework are included in Nikolov *et al.* [34]. This is a fundamental step, as former studies showed that an accurate control of the magnetization disorder is necessary in order to capture the experimentally observed changes in the magnetization and thereby recover the correct temperature-dependent elastic properties in spin-lattice calculations [34,37]. Assuming cubic symmetry, the relation between the elastic coefficients and stress/strain is illustrated in Eq. (6) [38],

$$\sigma_i = \sum_j c_{ij}\epsilon_j. \tag{6}$$

By applying the strain profile shown in Eq. (7), where $\eta = 0.02L$ and L is the simulation box length [$L = 20V(T)^{1/3}$], the elastic coefficients $c_{11}(T)$, $c_{12}(T)$, and $c_{44}(T)$ can be determined as shown in Eqs. (8)–(10),

$$\epsilon(\eta) = \begin{bmatrix} \eta & \eta/2 & 0.0 \\ \eta/2 & 0.0 & 0.0 \\ 0.0 & 0.0 & 0.0 \end{bmatrix}, \tag{7}$$

$$\frac{d\sigma_{xx}(T)}{d\eta} = c_{11}(T), \tag{8}$$

$$\frac{d\sigma_{yy}(T)}{d\eta} = c_{12}(T), \tag{9}$$

$$\frac{d\sigma_{xy}(T)}{d\eta} = c_{44}(T). \tag{10}$$

After deforming the simulation cell, the system is relaxed for 3 ps. Once this is done, the stresses ($\sigma_{xx}, \sigma_{yy}, \sigma_{xy}$) are averaged for 2 ps using a sampling frequency of 0.001 ps. This procedure is repeated using 10 different random seeds in the lattice/spin thermostats. The reported values in Figs. 3(b) and 4(b) reflect these sample averages.

To extract the magnetoelastic constants (B_1 and B_2), each of the 16 000 atom cells is first equilibrated at the appropriate magnetization. Once this is done, we extract 10 atomic configurations from each cell. Freezing the atoms in each of these configurations, we then rotate the spins 90° in the $x - z$ plane, in 5° increments, without disturbing the relative orientation between neighboring spins. This allows us to map the angular dependence of the magnetocrystalline anisotropy energy and to compute its maximum. Figure SF.1 in the Supplemental Material shows how the magnetic energy varies with the rotation angle of the spins [28]. We note that the frozen configurations are equilibrated to the correct temperature and magnetization at approximately 0 GPa, thereby retaining the correct atomic and magnetic disorder.

As illustrated in Table I, the interatomic SNAP potential reproduces the c_{11}, c_{12}, and c_{44} elastic coefficients and the DFT equilibrium volume well. In addition, the zero-temperature parametrization of the Néel potential successfully recovers the experimentally observed K_1, B_1, and B_2 values.

TABLE I. Zero-Kelvin properties obtained with our magnetoelastic machine-learned interatomic potential following the DAKOTA optimization [34] with ground truth values taken from DFT calculations or experiments [39,40].

	SNAP	Expt/DFT	Units	Error %
V_0	22.67	22.67	Å^3	0.03%
c_{11}	254.61	239.55	GPa	6.29%
c_{12}	135.65	138.1	GPa	2.68%
c_{44}	106.14	120.75	GPa	13.76%
K_1	53.0	55.0	MJ/m^3	3.63%
B_1	−3.73	−3.74	MJ/m^3	0.17%
B_2	10.18	11.2	MJ/m^3	9.11%

III. RESULTS AND DISCUSSION

Figure 1 illustrates the magnetocrystalline anisotropy energy surfaces which the zero-temperature Néel parametrization produces. In Fig. 1(a), the changes in the magnetocrystalline anisotropy energy surfaces with uniaxial strain are illustrated, where positive values of strain denote compression and negative values denote tension. Meanwhile, the images in Fig. 1(b) illustrate the changes in the magnetocrystalline anisotropy energy surface with shear strain. The x values underneath each graphic denote the maximum magnetocrystalline anisotropy energy (in units of μeV) for that surface. In all cases, it can be seen that deformations increase the magnetocrystalline anisotropy energy. We note that the zero-temperature parametrization produces the expected cubic anisotropy at 0 K. For uniaxial strains, compression causes the magnetocrystalline anisotropy energy surface to switch to an easy-axis configuration, whereas tension causes the magnetocrystalline anisotropy energy surface to transition to an easy-plane configuration. In shear, interestingly, the energy peaks near the obtuse angles of the deformed cell become attenuated, whereas the energy peaks at the acute angles of the cell are amplified. For large shear strains, ultimately, the magnetocrystalline anisotropy energy surfaces switches to an easy-plane configuration which is aligned along the cell diagonal. Figure 1 highlights the unique magnetocrystalline coupling that the Néel interactions enable. As will be illustrated in the paragraphs that follow, measurements for B_1 and B_2 are performed by tracking how the magnetocrystalline anisotropy energy surface changes with strain locally (at 45° for B_1 and 0° for B_2 in the $x - z$ plane).

Figure 2 displays our first set of obtained measurements. The PCMCC approach described in Nikolov *et al.* [34] enables a precise control of the pressure and magnetization at a given temperature. This step is crucial, as former studies showed that thermoelastic properties cannot be accurately computed without a good control of the magnetization, which needs to closely follow the experimental values [34]. Figure 2(a) shows the obtained magnetization versus temperature trend, where excellent agreement with the experimental data is observed.

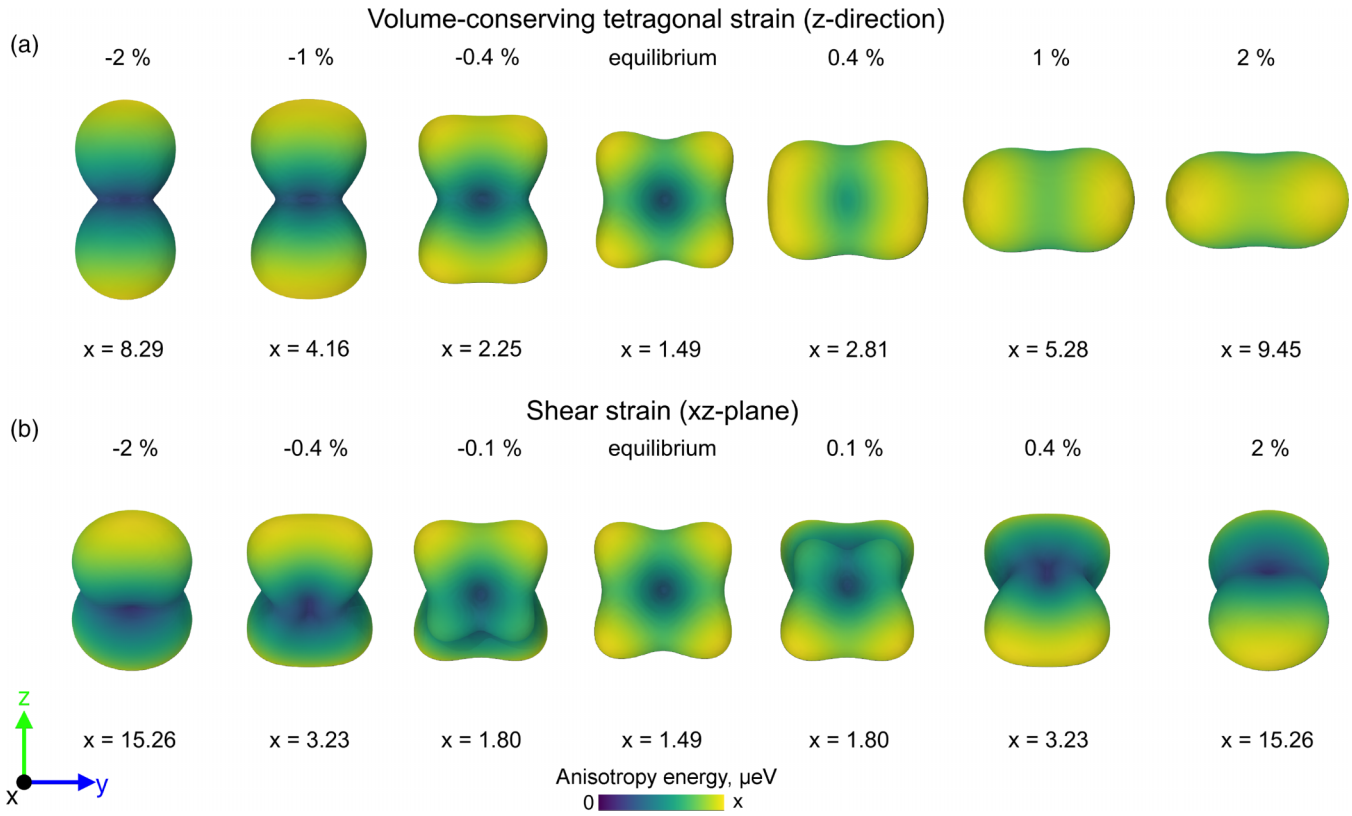

FIG. 1. (a) Anisotropy energy surfaces obtained by applying volume-conserving tetragonal strains to the crystal cell. Negative strain denotes tension and positive strain denotes compression along the z direction. Under tension, the magnetic anisotropy transitions to a lower-order easy-plane uniaxial configuration. Similarly, for compression, the anisotropy changes to a lower-order easy-axis uniaxial equilibrium state. (b) At 0 K, shearing the sample attenuates the anisotropy peaks near the obtuse angles of the cell. With increasing shear strain, the peaks near the obtuse angles are eliminated and the magnetocrystalline anisotropy energy surfaces switch to an easy-plane configuration. This easy-plane configuration is aligned along the cell diagonal that connects the two acute angle corners of the cell.

The MSD simulations account for thermal expansion, thus allowing the cell volume to expand/contract with temperature, as displayed by Fig. 2(b). Our model predicts an excellent thermal expansion coefficient up to approximately 750 K. When the system's temperature approaches the Curie transition (here between 750 and 1045 K), our model shows a departure from experimental volume-expansion trends. This seems to indicate that the magnetic component of the pressure, generated by the magnetic disorder of the system, is amplified in the current MSD model.

Controlling both the magnetization and pressure of the system allows us to compute the temperature dependence for the first magnetocrystalline anisotropy coefficient [23]. Its value is obtained by measuring the changes in energy when the spins are rotated in the $x-z$ plane. Figure 2(c) displays the obtained averaged values. Excellent agreement is recovered with experimental measurements and with the empirical Callen law [44].

To evaluate the magnetoelastic coefficient B_1, as well as the corresponding magnetostriction coefficient λ_{100}, we apply a series of volume-conserving tetragonal deformations ($\epsilon_{xx} = \epsilon_{yy} = -\epsilon_{zz}/2$), following the approach described in Marchant *et al.* [24]. We vary ϵ_{zz} between approximately -1% and 1% of the simulation box. For each deformation, the spins are rotated 90° (in 5° increments) in the $x-z$ plane and the associated energy fluctuations are measured. The magnetic torque, corresponding to $-dE_{me}/d\theta$, can then be computed at an angle of 45° (here corresponding to a [101] orientation of the magnetization). This process allows us to measure the variation of the torque at 45° as a function of lattice strain. Examples of torque versus strain plots are provided in Fig. SF.2 of the Supplemental Material [28]. As shown in Fig. SF.2, for a given temperature, the corresponding slope ($-dE_{me}/d\theta$ vs strain) is constant, and its value provides us with the first magnetoelastic coefficient B_1.

Figure 3(a) displays the temperature dependence of B_1 as obtained by the MSD model using the zero-temperature Néel parametrization. Finite-temperature measurements of the elastic constants are carried out following the approach detailed in Sec. II. Figure 3(b) shows the obtained values for $(c_{11}-c_{12})/2$. The first magnetostriction coefficient is defined as

$$\lambda_{100} = -\frac{2}{3}\frac{B_1}{c_{11}-c_{12}} \tag{11}$$

and can thus be evaluated from the former results. Figure 3(c) displays the obtained λ_{100} temperature dependence results.

As can be observed in Figs. 3(a) and 3(c), using the zero-temperature Néel parametrization, we recover good agreement with experiments up to 500 K. However, the zero-temperature parametrization is not able to capture the well-known anomaly of B_1 and λ_{100}, i.e., the second maximum occurring around 800 K [42]. In their recent work,

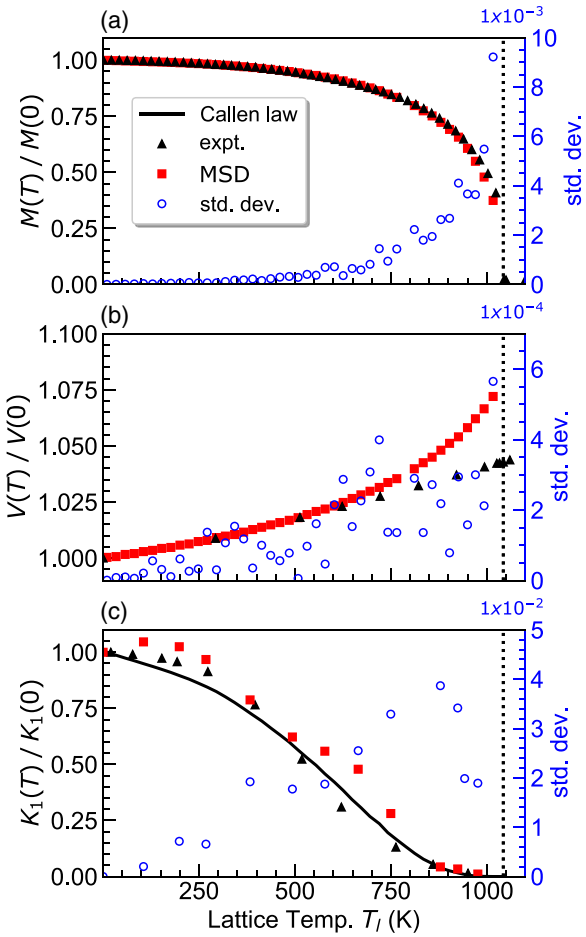

FIG. 2. (a) Average magnetization norm as a function of temperature in the pressure- and magnetization-controlled conditions (PCMCC) as defined in Nikolov *et al.* [34]. (b) Per-atom volume as a function of temperature. (c) Measurement of the magnetic anisotropy constant. Experimental data are extracted from Refs. [41–43].

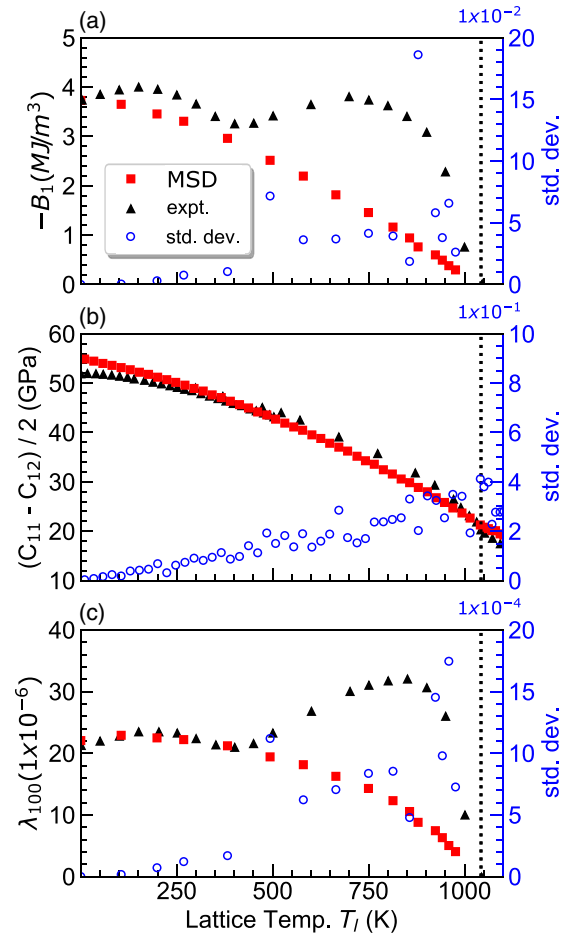

FIG. 3. (a) Temperature dependence of the first magnetoelastic coefficient B_1. (b) The evolution of the first shear constant, $(c_{11} - c_{12})/2$. (c) Changes in magnetostriction coefficient λ_{100} with temperature.

Marchant *et al.* showed that *ab initio* calculations within the disordered local moment picture for bcc Fe can correctly reproduce the second peak at high temperature of B_1 ($T \simeq 800$ K) for some particular values of the lattice parameter [24]. This seems to indicate that part of the physical mechanism responsible for the second peak is present in the *ab initio* formalism, but absent from the 0 K Néel implementation. Callen and Callen indicated that this second peak might be related to the existence of an asymmetry in the excitation of the magnon spectrum, which could be caused by dipolar spin interactions [42]. Future investigation could consider more sophisticated anisotropic exchange Hamiltonians [45,46], as well as overlaying long-range dipole-dipole interactions to our model.

We also evaluate the ability of our model to compute the second magnetoelastic coefficient B_2, as well as the corresponding magnetostriction coefficient λ_{111}. To do so, we develop a simple procedure analogous to the one presented by Marchant *et al.* [24], but applied to shear deformation. For an applied strain in the $x - z$ plane, the magnetoelastic energy as a function of magnetization orientation and shear deformation can be written as

$$E_{me} = \frac{B_2}{2}\epsilon_{xz}\sin(2\theta). \tag{12}$$

We vary ϵ_{xz} between -1 to 1% of the simulation box. The same spin rotations (as described for the B_1 calculation above) are applied, also within the $x - z$ plane. For a given temperature, the second magnetoelastic coefficient can be computed by evaluating the magnetic torque at a 0° angle as a function of lattice strain, as described by the following equation:

$$T(\theta = 0) = B_2\epsilon_{xz}. \tag{13}$$

Figure 4(a) displays our obtained B_2 measurements as a function of temperature. Despite recovering the correct sign and initial value, the zero-temperature parametrization does not capture the curvature of the experimental B_2 trend [43], which follows the power law $B_2(T)/B_2(0) = [M(T)/M(0)]^{14}$. Following the approach detailed in Sec. II, the shear elastic constant c_{44} is evaluated and displayed in Fig. 4(b). The second magnetostriction coefficient is defined as

$$\lambda_{111} = -\frac{1}{3}\frac{B_2}{c_{44}}. \tag{14}$$

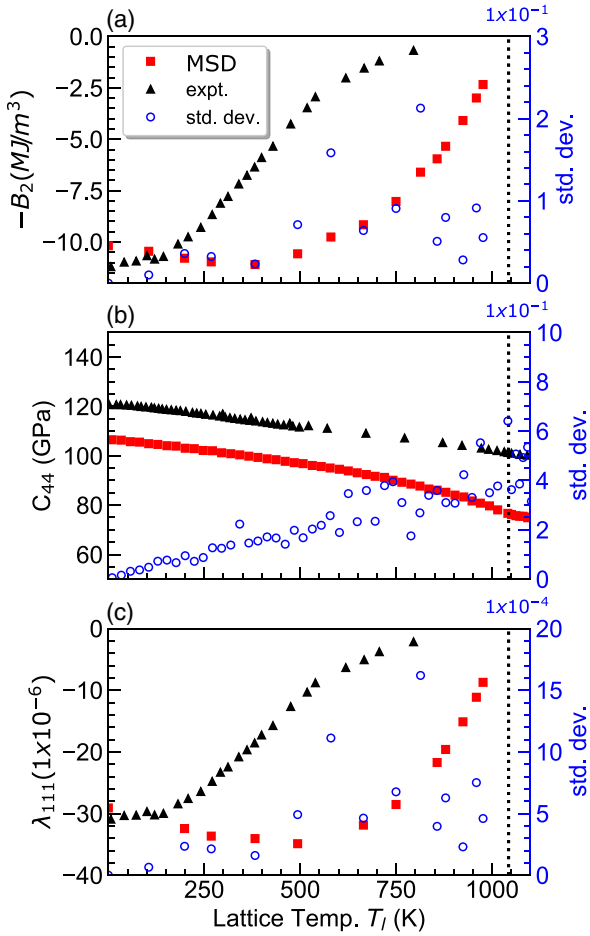

FIG. 4. (a) Temperature dependence of the second magnetoelastic coefficient B_2. (b) The evolution of the second shear constant, c_{44}. (c) Changes in magnetostriction coefficient λ_{111} with temperature.

The corresponding results for λ_{111} are displayed in Fig. 4(c). The trend of λ_{111} follows B_2: its sign as well as initial and final values are in agreement with experiments, but the approach to zero is delayed until approximately 600 K, compared to approximately 200 K in experiments.

A detailed analysis of the 0 K parametrization of the Néel potential (and underlying assumptions) is shown in the work of Nieves *et al.* [23]. In order to better understand how the different Néel parameters impact the B_1 and B_2 magnetoelastic coefficients at finite temperature, we carry out δ moment-independent sensitivity analysis using the SALib PYTHON library [47]. The δ moment-independent sensitivity analysis examines how different Néel parameters impact the probability density functions for B_1 and B_2 coefficients [48–50]. A schematic illustrating the sensitivity analysis calculations is shown in Fig. SF.4 of the Supplemental Material [28] and additional details regarding the calculations are also provided in Appendix C. The sensitivity analysis study conducted here used approximately 32 000 sample points. The δ coefficients for both the total sensitivities and first-order sensitivities are shown in Fig. 5. The plot in Fig. 5(a) shows that the impact of r_{cut} and l_δ on the B_1 coefficient increases significantly at higher temperatures. The parameters r_{cut} and l_δ are both

TABLE II. Néel parameters space explored by genetic algorithm and δ moment-independent sensitivity analysis.

Parameter	Lower bound	Upper bound
R_c	2.0	3.2
$l(r_{ij})_\alpha$	1×10^{-4}	8×10^{-4}
$l(r_{ij})_\gamma$	0.1	3.5
$l(r_{ij})_\delta$	0.1	7.0
$q(r_{ij})_\alpha$	5×10^{-6}	8×10^{-5}
$q(r_{ij})_\gamma$	0.05	3.5
$q(r_{ij})_\delta$	0.1	7.0

distances, where in the 0 K parametrization l_δ is the nearest-neighbor distance.

At finite temperatures, a small increase in the impact of q_a, q_b, and q_c is also observed. The first-order sensitivities make up a small portion of the total δ sensitivity, indicating that higher-order interactions between different Néel parameters dominate. For the first-order sensitivity of B_1 [Fig. 5(c)], r_{cut} is the only dominant parameter near 0 K. At higher temperatures, the B_1 probability distribution becomes more sensitive to the l_γ and l_δ parameters.

For the B_2 coefficient [Fig. 5(b)], the total δ sensitivity of the different Néel parameters does not change significantly with temperature. The parameters r_{cut} and l_δ are found to be dominant throughout the entire 0–1000 K range. The first-order sensitivity of B_2 [Fig. 5(d)] is more sensitive to temperature. At higher temperatures for both r_{cut} and l_δ, a significant increase in the first-order sensitivity is observed. For B_2, the impact of higher-order interactions between parameters is also lessened at higher temperatures, as first-order interactions make up a larger portion of the total sensitivity. The B_1 and B_2 first-order sensitivities do not appear to be impacted strongly by the l_α, q_α, q_γ, q_δ parameters. In general, once the total δ sensitivity at finite temperatures begins to vary significantly, we begin reaching the limits of the 0 K parametrization. Thus, from Fig. 6, one would expect B_1 to benefit most from a finite-temperature parametrization, whereas a reparameterization at higher temperatures may not yield significant improvements for B_2 over the 0–1200 K range.

We utilize the moment-independent sensitivity analysis data to initialize a genetic algorithm (using DAKOTA software) that tries to satisfy objective functions for $B_1(T_l)$, $B_2(T_l)$, and K_1 (0 K), which are calculated based on rotations in the $x-z$ plane. For the genetic algorithm search, we employ a population size of 300 candidates. The genetic algorithm search is carried out over the same parameter space spanned in the sensitivity analysis, which is shown in Table II. Results for the genetic algorithm optimized potential after 1000 iterations are shown in Fig. 6, which shows results for both λ_{100} and λ_{111}. The results for λ_{100} match experiments very closely up to approximately 300 K. At higher temperatures, we no longer observed the monotonic decrease which was seen in Fig. 3(c). Hence, we are importantly able to capture the high-temperature peak of λ_{100} which occurs near 800 K. The peak value of λ_{100} is overestimated by approximately 30% however. The genetic algorithm optimized potential also

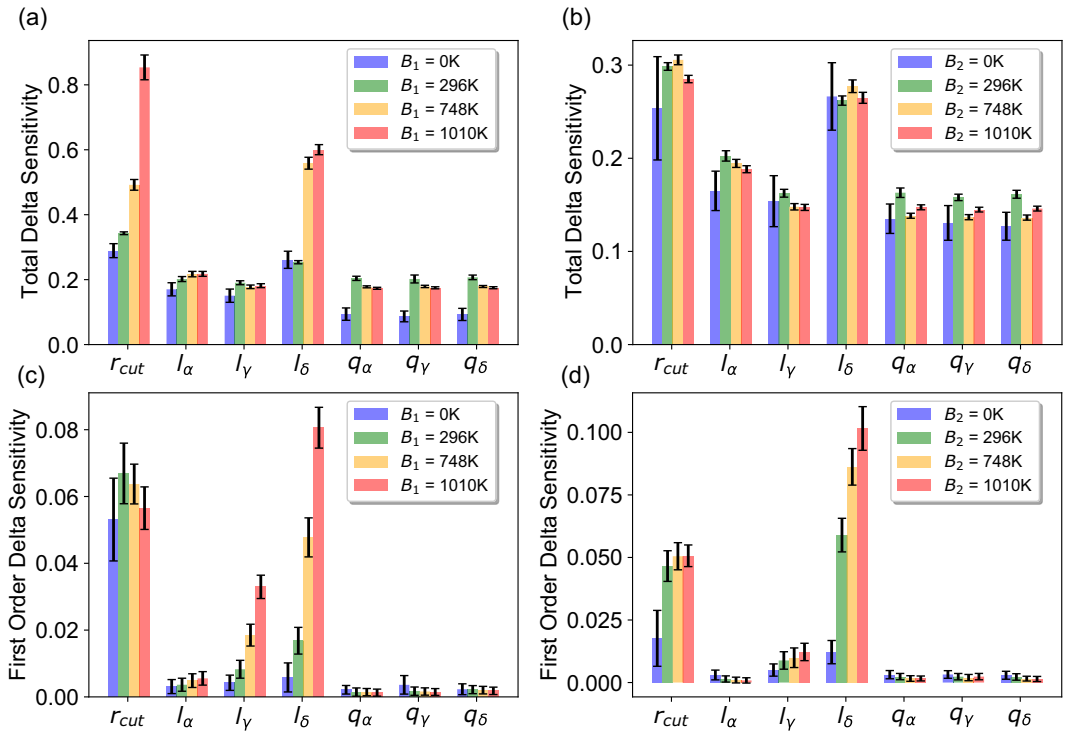

FIG. 5. (a),(b) The total δ (moment-independent) sensitivities for B_1 and B_2. (c),(d) First-order δ sensitivities for B_1 and B_2. Error bars are based on 95% confidence intervals.

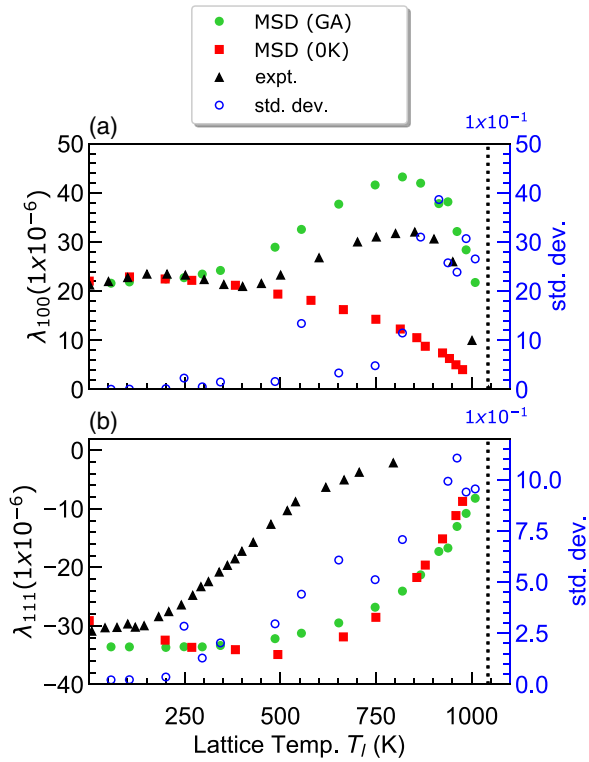

FIG. 6. (a),(b) Changes in magnetostriction coefficients λ_{100} and λ_{111} with temperature for the 0 K and genetic algorithm (GA) model parameters shown in Table III.

slightly improves the results for λ_{111}. By comparing to the data in Fig. 4(c), we can see that λ_{111} now monotonically increases towards the Curie temperature, and we no longer observe a slight decrease in λ_{100} in the range of 0–500 K. The curvature of the MSD data, however, still deviates from experiments, where again λ_{111} does not begin to significantly change until approximately 600 K. The value of K_1 (0 K) for the genetic algorithm optimized potential is found to be 44 MJ/m^3, which represents a deviation of approximately 20% from the experimental value of 55 MJ/m^3.

IV. CONCLUSION

We presented a molecular-spin dynamics framework that features a two-way coupling between the orientation of the magnetic moment vector and lattice strain. As shown, this coupling scheme, represented by the Néel interaction model, enables us to naturally capture changes in the magnetocrystalline energy surfaces with strain (Fig. 1). To gauge our ability to reproduce experimental λ_{100} and λ_{111} coefficients, we utilized a quantum-accurate SNAP interatomic potential which was trained to reproduce the c_{11}, c_{12}, and c_{44} elastic constants within the 0–1200 K range using the PCMCC framework [34]. Initially, we applied a 0 K parametrization of the Néel interaction parameters following the procedure outlined in Nieves *et al.* [23]. Doing this, we observed that both λ_{100} and λ_{111} are captured very well at 0 K. At finite temperatures, the λ_{100} coefficient was captured well up to ∼500 K; however, the second peak in λ_{100}, which occurred near 800 K, could not be reproduced. The λ_{111} calculations agreed with experiments up to ∼250 K.

Applying a δ moment-independent sensitivity analysis [48], we examined how the different Néel parameters impact the probability density functions for the B_1 and B_2 coefficients, where we found the total δ sensitivity of B_1 to be more significantly impacted at higher temperatures compared to B_2, which showed negligible sensitivity to temperature. Using the dataset from the sensitivity analysis, we then initiated a genetic algorithm search over the Néel interaction parameters in order to minimize the error in the B_1 and B_2 coefficients at higher temperatures. This finite-temperature parametrization allowed us to reproduce the second peak in the λ_{100} coefficient, highlighting that the Néel model can indeed reproduce some of the high-temperature nonmonotonic magnetoelastic behavior of iron. The genetic algorithm parametrization, however, only mildly improved the agreement in the λ_{111} coefficient. The fact that the total δ sensitivity for B_2 did not significantly change at higher temperatures (like B_1) perhaps explains why the results for the genetic algorithm and 0 K parametrization did not vary as drastically.

While the temperature dependence of magnetostriction for localized magnetism has been well characterized theoretically [51], extending those efforts to itinerant magnetic materials such as bcc Fe is quite challenging. We point out that the used spin-lattice model in this work is based on the two-ion Hamiltonian and may be more realistic for localized magnetism rather than for itinerant magnetism, where a band model could be more appropriate. For example, Ohta and Shimizu [53] found that B_2 seems to be more sensitive to details of band structure than B_1 for bcc Fe, which is consistent with the stronger temperature dependence of B_2 as compared with that of B_1. This fact might also explain why the genetic algorithm parametrization reproduced the temperature dependence of B_1 better than B_2. We do also note that in the current effort, we assumed that all spins have a fixed magnetic moment (2.2 Bohr magnetons). In reality, the magnetic moment of each atom will fluctuate with pressure and temperature. Hence, at each temperature, there will be an associated distribution of magnetic moments. As the temperature increases, the magnetic moment distribution will widen and the behavior of the system will deviate more and more from the fixed-magnetic moment assumption. Gauging the impact of longitudinal spin fluctuations and exploring more sophisticated anisotropy models is something we hope to examine in our future work. Lastly, we do note that the theoretical approach described in Nieves *et al.* [23] is orders of magnitude faster than the genetic algorithm optimization, which requires significantly higher computational resources. Hence, the genetic algorithm optimization is more suited for high-temperature regimes where the ground-state (0 K) approach in Ref. [23] may struggle. While the present study focuses on bcc iron, the methods described here are completely general (only based on *ab initio* results), and could be directly transposed to any material of interest.

ACKNOWLEDGMENTS

This article has been authored by an employee of National Technology & Engineering Solutions of Sandia, LLC under Contract No. DE-NA0003525 with the U.S. Department of Energy (DOE). The employee owns all right, title, and interest in and to the article and is solely responsible for its contents. The U.S. Government retains and the publisher, by accepting the article for publication, acknowledges that the U.S. Government retains a nonexclusive, paid-up, irrevocable, worldwide license to publish or reproduce the published form of this article or allow others to do so, for U.S. Government purposes. The U.S. DOE will provide public access to these results of federally sponsored research in accordance with the U.S. DOE Public Access Plan [52]. This work was supported by the ERDF in the IT4Innovations national supercomputing center - path to exascale project (Grant No. CZ.02.1.01/0.0/0.0/16-013/0001791) within the OPRDE and projects "e-INFRA CZ (ID90140)" and Donau No. 8X20050 by The Ministry of Education, Youth and Sports of the Czech Republic.

APPENDIX A: MAGNETOELASTIC HAMILTONIAN

The magnetic component of the spin-lattice Hamiltonian [Eq. (3)] contains two magnetoelastic contributions, the exchange interaction and a Néel model.

Former studies discussed the improved accuracy in representing magnetic excitation in 3D transition ferromagnets by adding a biquadratic term to the standard Heisenberg Hamiltonian [32,54]. Our exchange interaction model follows those approaches:

$$\mathcal{H}_{\text{ex}} = -\sum_{i\neq j}^{N} J\left(r_{ij}\right)\left[\boldsymbol{s}_i \cdot \boldsymbol{s}_j - 1\right] - \sum_{i\neq j}^{N} K\left(r_{ij}\right)\left[(\boldsymbol{s}_i \cdot \boldsymbol{s}_j)^2 - 1\right], \tag{A1}$$

where $\boldsymbol{s}_i$ and $\boldsymbol{s}_j$ are classical atomic spins of unit length located on atoms i and j, $J(r_{ij})$ and $K(r_{ij})$ (in eV) are magnetic exchange functions, and r_{ij} is the interatomic distance between magnetic atoms i and j. The two terms in Eq. (A1) are offset by subtracting the spin ground state (corresponding to a purely ferromagnetic situation), as detailed in Ma *et al.* [55]. Although this offset of the exchange energy does not affect the precession dynamics of the spins, it allows one to offset the corresponding mechanical forces. Without this additional term, the magnetic contribution to the forces and the pressure are not zero at the energy ground state. Details about this exchange model and its parametrization on first-principles results can be found in the Methods section of Nikolov *et al.* [34].

The second magnetoelastic contribution to our model aims to represent effects arising from the spin-orbit coupling. We use a biquadratic Néel pair interaction defined as follows:

$$\begin{aligned}\mathcal{H}_{\text{Néel}} = -\frac{1}{2}\sum_{i,j=1,i\neq j}^{N} & l_1(r_{ij})\left[(\boldsymbol{e}_{ij}\cdot\boldsymbol{s}_i)(\boldsymbol{e}_{ij}\cdot\boldsymbol{s}_j) - \frac{\boldsymbol{s}_i\cdot\boldsymbol{s}_j}{3}\right] \\ & + q_1(r_{ij})\left[(\boldsymbol{e}_{ij}\cdot\boldsymbol{s}_i)^2 - \frac{\boldsymbol{s}_i\cdot\boldsymbol{s}_j}{3}\right]\left[(\boldsymbol{e}_{ij}\cdot\boldsymbol{s}_j)^2 - \frac{\boldsymbol{s}_i\cdot\boldsymbol{s}_j}{3}\right] \\ & + q_2(r_{ij})[(\boldsymbol{e}_{ij}\cdot\boldsymbol{s}_i)(\boldsymbol{e}_{ij}\cdot\boldsymbol{s}_j)^3 + (\boldsymbol{e}_{ij}\cdot\boldsymbol{s}_j)(\boldsymbol{e}_{ij}\cdot\boldsymbol{s}_i)^3],\end{aligned} \tag{A2}$$

where $\boldsymbol{e}_{ij} = \boldsymbol{r}_{ij}/r_{ij}$, and $l_1(r_{ij})$, $q_1(r_{ij})$, and $q_2(r_{ij})$ are three functions defining the magnitude and fluctuations of the

TABLE III. Exchange and Néel parameters of interaction model. For the Néel dipole and quadrupole terms we consider two different sets of parameters, one is derived theoretically at zero-kelvin (0 K) using a short-range interactive model [23], and the other one is obtained numerically using a genetic algorithm (GA).

Method	Type	α (eV)	γ	δ (Å)	R_c (Å)
Exchange [34]	J(r_{ij})	0.2827	−4.747	0.781	5.0
Exchange [34]	K(r_{ij})	−0.03619	−2.973	0.5273	5.0
0 K [23]	l(r_{ij})	3.773×10^{-4}	0.7898	2.4511	2.6
0 K [23]	q(r_{ij})	2.997×10^{-5}	1.0496	2.4511	2.6
GA [48]	l(r_{ij})	6.007×10^{-4}	1.0436	1.1967	3.09
GA [48]	q(r_{ij})	4.163×10^{-5}	2.1784	5.8348	3.09

interaction. The dot products between spins and lattice vectors $\boldsymbol{e}_{ij}$ provide the model with a direct coupling between the magnetic energy and direction of magnetization. A collinear spin approximation allows one to express the three functions in terms of two functions only,

$$\begin{aligned} l_1(r_{ij}) &= l(r_{ij}) + \tfrac{12}{35}q(r_{ij}), \\ q_1(r_{ij}) &= \tfrac{9}{5}q(r_{ij}), \\ q_2(r_{ij}) &= -\tfrac{2}{5}q(r_{ij}). \end{aligned} \tag{A3}$$

This leaves us with four functions of the interatomic distance r_{ij}: $J(r_{ij})$, $K(r_{ij})$, $l(r_{ij})$, and $q(r_{ij})$. A Bethe-Slater form is chosen for their lattice dependence [56,57],

$$f(r) = 4\alpha\left(\frac{r}{\delta}\right)^2\left[1-\gamma\left(\frac{r}{\delta}\right)^2\right]e^{-\left(\frac{r}{\delta}\right)^2}\Theta(R_c - r), \tag{A4}$$

where α denotes the interaction energy, δ the interaction decay length, γ a dimensionless curvature parameter, $r = r_{ij}$ the radial distance between atoms i and j, and $\Theta(R_c - r)$ a Heaviside step function for the radial cutoff R_c. This assumes that the interaction decays rapidly with the interatomic distance, consistent with former calculations [32,58].

The two functions corresponding to the exchange interaction are parametrized to recover first-principles spin-spiral results. The spin-spiral results were obtained leveraging the VASP package [35]. The approach and the associated results are detailed in the Methods section of Nikolov *et al.* [34]. The parameters of the two Néel interaction functions, $l(r_{ij})$, and $q(r_{ij})$, are obtained using the method described in Ref. [23]. They are parameterized to recover the experimental values of the magnetocrystalline anisotropy and the magnetoelastic coefficients. Table III summarizes the obtained parameters and radius cutoffs of the four functions.

APPENDIX B: SNAP POTENTIAL

This work utilized a quadratic model form of the SNAP interatomic potential that was specifically parameterized for the molecular-spin dynamics framework described here. The SNAP potential utilizes the bispectrum descriptors, developed by Bartok *et al.* [59,60], to describe the local environment of each atom. As previously shown, the quadratic SNAP implementation can be derived by including an embedding energy term into the linear SNAP energy expression [61]. Expressing this embedding energy as a Taylor expansion allows us to extend the linear SNAP energy expression to include all distinct pairwise products of the bispectrum components $\mathbf{B}_i$. The SNAP energy of a given atom can then be represented as a function of the K bispectrum components, as shown in Eq. (B1),

$$E^i_{\mathrm{SNAP}}(\mathbf{r}^{\mathbf{N}}) = \boldsymbol{\beta}\cdot\boldsymbol{B}_i + \tfrac{1}{2}(\boldsymbol{B}_i)^T\cdot\boldsymbol{\alpha}\cdot\boldsymbol{B}_i. \tag{B1}$$

Here, $\boldsymbol{\alpha}$ is a symmetric $K\times K$ matrix consisting of constant coefficients corresponding to products of descriptors. Meanwhile, $\boldsymbol{\beta}$ is a vector of constant coefficients for the linear combination of descriptors. Both $\boldsymbol{\alpha}$ and $\boldsymbol{\beta}$ are determined during training, via linear regression without sparsity or higher moment penalties in the loss function. The bispectrum components can be expressed as the Clebsch-Gordan product of 4D-hyperspherical harmonics, $\boldsymbol{U_j}$, as shown in Eq. (B2),

$$B_{j_1 j_2 j} = \boldsymbol{U_{j_1}} \otimes^j_{j_1 j_2} \boldsymbol{U_{j_2}} : \boldsymbol{U_j}^*. \tag{B2}$$

The forces on each atom can then be expressed as a weighted sum of the bispectrum derivatives with respect to $\boldsymbol{r_j}$, as shown in Eq. (B3),

$$F^j_{\mathrm{SNAP}} = -\nabla_j \sum_{i=1}^{N} E^i_{\mathrm{SNAP}} = -\boldsymbol{\beta}\cdot\sum_{i=1}^{N}\frac{\partial \boldsymbol{B}_i}{\partial \boldsymbol{r_j}}. \tag{B3}$$

Using linear regression to pin down both $\boldsymbol{\alpha}$ and $\boldsymbol{\beta}$, one can then determine the corresponding energies/forces/stresses for each DFT configuration taken as training. Within the genetic algorithm implementation of DAKOTA, we also vary the energy/force/stress weights for different training groups to provide extra flexibility to training these models. The energy and force errors serve as objective functions for each genetic algorithm evaluation. In addition, we also introduce extra objective functions during optimization which gauge the finite-temperature elastic properties as well as bcc/hcp lattice constants and cohesive energies of different crystal phases at 0 K. Detailed information regarding how the training groups and objective functions are set up is included in Nikolov *et al.* [34]. The finalized potential is available in the Fe_Quad directory of Ref. [62], and includes the α, β coefficients.

APPENDIX C: δ MOMENT-INDEPENDENT SENSITIVITY ANALYSIS

The δ sensitivity analysis applied here is a global approach which examines how individual parameters alter the probability distribution of a quantity of interest, in this case B_1/B_2. This approach is different from variance-based approaches, such as the Sobol sensitivity analysis, where the sensitivity of a particular moment (the variance) is examined. In general, previous works have shown that inputs which variance-based approaches regard as important do not necessarily make a large impact on the output uncertainty distribution [49]. Thus to better understand how individual Néel parameters impact the entire output distributions of B_1/B_2, we focus on the δ moment-independent sensitivity analysis. By understanding how temperature impacts the sensitivity of B_1/B_2 to individual Néel parameters, we can gauge when a reparameterization of the Néel model is appropriate. In the δ sensitivity analysis,

the importance of a given input X_l (Néel parameter) can be described by Eq. (C1) shown below,

$$\delta_l = \tfrac{1}{2} E_{X_l}[s(X_l)]. \tag{C1}$$

Here, $s(X_l)$ is given by Eq. (C2), where $f_Y(y)$ is the density of the output and $f_{Y|X_l}$ is the conditional density of the output assuming that X_l is fixed constant at $X_l = x$. The function $s(X_l)$ then specifies the area between $f_Y(y)$ and $f_{Y|X_l}$,

$$s(X_l) = \int |f_Y(y) - f_{Y|X_l}(y)| dy. \tag{C2}$$

If $s(X_l)$ is known, then $E_{X_l}[s(X_l)]$ can be defined as shown in Eq. (C3) below, where $f_{X_l}(x_l)$ is the density of the input X_l,

$$E_{X_l}[s(X_l)] = \int f_{X_l}(x_l) \left[\int |f_Y(y) \ldots - f_{Y|X_l}(y)| dy \right] dx_l. \tag{C3}$$

Additional details on the δ sensitivity analysis approach are included in the works of Borgonovo *et al.* [48–50].

[1] E. Callen, J. Appl. Phys. **39**, 519 (1968).
[2] N. Ekreem, A. Olabi, T. Prescott, A. Rafferty, and M. Hashmi, J. Mater. Process. Technol. **191**, 96 (2007).
[3] E. W. Lee, Rep. Prog. Phys. **18**, 184 (1955).
[4] A. Bur, T. Wu, J. Hockel, C.-J. Hsu, H. K. Kim, T.-K. Chung, K. Wong, K. L. Wang, and G. P. Carman, J. Appl. Phys. **109**, 123903 (2011).
[5] Y. Yao, Y. Pan, and S. Liu, Ultrasonics Sonochemistry **62**, 104722 (2020).
[6] M. Dapino, *Encyclopedia of Smart Materials* (Wiley, New York, 2000).
[7] M. A. Weiss, A. Herbst, J. Schlegel, T. Dannegger, M. Evers, A. Donges, M. Nakajima, A. Leitenstorfer, S. T. B. Goennenwein, U. Nowak *et al.*, arXiv:2301.02006.
[8] T. Leonard, S. Liu, M. Alamdar, H. Jin, C. Cui, O. G. Akinola, L. Xue, T. P. Xiao, J. S. Friedman, M. J. Marinella *et al.*, Adv. Electron. Mater. **8**, 2200563 (2022).
[9] W. H. Brigner, N. Hassan, X. Hu, C. H. Bennett, F. Garcia-Sanchez, M. J. Marinella, J. A. C. Incorvia, and J. S. Friedman, in *2022 IEEE International Symposium on Circuits and Systems (ISCAS)*, (IEEE, New York, USA, 2022), pp. 1189–1193.
[10] L. Winter, S. Großenbach, U. Nowak, and L. Rózsa, Phys. Rev. B **106**, 214403 (2022).
[11] C.-Y. Liang, S. M. Keller, A. E. Sepulveda, W.-Y. Sun, J. Cui, C. S. Lynch, and G. P. Carman, J. Appl. Phys. **116**, 123909 (2014).
[12] S. Tehrani, B. Engel, J. Slaughter, E. Chen, M. DeHerrera, M. Durlam, P. Naji, R. Whig, J. Janesky, and J. Calder, IEEE Trans. Magn. **36**, 2752 (2000).
[13] P.-W. Ma and S. Dudarev, *Handbook of Materials Modeling: Methods: Theory and Modeling* (Springer International Publishing, Cham, Switzerland, 2020), pp. 1017–1035.
[14] D. Beaujouan, P. Thibaudeau, and C. Barreteau, Phys. Rev. B **86**, 174409 (2012).
[15] H. Lange, S. Mankovsky, S. Polesya, M. Weißenhofer, U. Nowak, and H. Ebert, arXiv:2302.02066.
[16] S. Mankovsky, S. Polesya, H. Lange, M. Weißenhofer, U. Nowak, and H. Ebert, Phys. Rev. Lett. **129**, 067202 (2022).
[17] E. Harris and J. Owen, Phys. Rev. Lett. **11**, 9 (1963).
[18] N. L. Huang and R. Orbach, Phys. Rev. Lett. **12**, 275 (1964).
[19] T. Strässle, F. Juranyi, M. Schneider, S. Janssen, A. Furrer, K. W. Krämer, and H.-U. Güdel, Phys. Rev. Lett. **92**, 257202 (2004).
[20] R. Zivieri, Symmetry **12**, 2061 (2020).
[21] D. Perera, M. Eisenbach, D. M. Nicholson, G. M. Stocks, and D. P. Landau, Phys. Rev. B **93**, 060402(R) (2016).
[22] M. Strungaru, M. O. A. Ellis, S. Ruta, O. Chubykalo-Fesenko, R. F. L. Evans, and R. W. Chantrell, Phys. Rev. B **103**, 024429 (2021).
[23] P. Nieves, J. Tranchida, S. Arapan, and D. Legut, Phys. Rev. B **103**, 094437 (2021).
[24] G. A. Marchant, C. E. Patrick, and J. B. Staunton, Phys. Rev. B **99**, 054415 (2019).
[25] C. E. Patrick, G. A. Marchant, and J. B. Staunton, Phys. Rev. Appl. **14**, 014091 (2020).
[26] P. Asselin, R. F. L. Evans, J. Barker, R. W. Chantrell, R. Yanes, O. Chubykalo-Fesenko, D. Hinzke, and U. Nowak, Phys. Rev. B **82**, 054415 (2010).
[27] P. Nieves, J. Tranchida, S. Nikolov, A. Fraile, and D. Legut, Phys. Rev. B **105**, 134430 (2022).
[28] See Supplemental Material at http://link.aps.org/supplemental/10.1103/PhysRevB.107.094426 for additional information regarding magnetoelastic calculations and sensitivity analysis.
[29] J. Tranchida, S. Plimpton, P. Thibaudeau, and A. Thompson, J. Comput. Phys. **372**, 406 (2018).
[30] A. P. Thompson, H. M. Aktulga, R. Berger, D. S. Bolintineanu, W. M. Brown, P. S. Crozier, P. J. in't Veld, A. Kohlmeyer, S. G. Moore, T. D. Nguyen *et al.*, Comput. Phys. Commun. **271**, 108171 (2022).
[31] A. P. Thompson, L. P. Swiler, C. R. Trott, S. M. Foiles, and G. J. Tucker, J. Comput. Phys. **285**, 316 (2015).
[32] A. Szilva, M. Costa, A. Bergman, L. Szunyogh, L. Nordström, and O. Eriksson, Phys. Rev. Lett. **111**, 127204 (2013).
[33] B. Zimmermann, G. Bihlmayer, M. Böttcher, M. Bouhassoune, S. Lounis, J. Sinova, S. Heinze, S. Blügel, and B. Dupé, Phys. Rev. B **99**, 214426 (2019).
[34] S. Nikolov, M. A. Wood, A. Cangi, J.-B. Maillet, M.-C. Marinica, A. P. Thompson, M. P. Desjarlais, and J. Tranchida, npj Comput. Mater. **7**, 153 (2021).
[35] G. Kresse and J. Hafner, Phys. Rev. B **47**, 558 (1993).
[36] B. M. Adams, W. J. Bohnhoff, K. Dalbey, J. Eddy, M. Eldred, D. Gay, K. Haskell, P. D. Hough, and L. P. Swiler, Tech. Rep. No. SAND2010-2183 (Sandia National Laboratories, Albuquerque, NM, 2009).
[37] R. F. L. Evans, U. Atxitia, and R. W. Chantrell, Phys. Rev. B **91**, 144425 (2015).
[38] P. Steneteg, O. Hellman, O. Y. Vekilova, N. Shulumba, F. Tasnádi, and I. A. Abrikosov, Phys. Rev. B **87**, 094114 (2013).

[39] J. J. Adams, D. Agosta, R. Leisure, and H. Ledbetter, J. Appl. Phys. **100**, 113530 (2006).
[40] M. Getzlaff, *Fundamentals of Magnetism* (Springer-Verlag Berlin, Heidelberg, Germany, 2007).
[41] D. Dragoni, D. Ceresoli, and N. Marzari, Phys. Rev. B **91**, 104105 (2015).
[42] H. B. Callen and E. R. Callen, Phys. Rev. **132**, 991 (1963).
[43] E. du Tremolet de Lacheisserie and R. Mendia Monterroso, J. Magn. Magn. Mater. **31-34**, 837 (1983).
[44] H. B. Callen and E. Callen, J. Phys. Chem. Solids **27**, 1271 (1966).
[45] V. Borisov, Y. O. Kvashnin, N. Ntallis, D. Thonig, P. Thunström, M. Pereiro, A. Bergman, E. Sjöqvist, A. Delin, L. Nordström *et al.*, Phys. Rev. B **103**, 174422 (2021).
[46] S. Streib, R. Cardias, M. Pereiro, A. Bergman, E. Sjöqvist, C. Barreteau, A. Delin, O. Eriksson, and D. Thonig, Phys. Rev. B **105**, 224408 (2022).
[47] J. Herman and W. Usher, J. Open Source Software **2**, 97 (2017).
[48] E. Borgonovo, W. Castaings, and S. Tarantola, Risk Anal.: Intl. J. **31**, 404 (2011).
[49] E. Borgonovo, Risk Anal. **26**, 1349 (2006).
[50] E. Borgonovo and S. Tarantola, Intl. J. Chem. Kinetics **40**, 687 (2008).
[51] E. du Trémolet de Lacheisserie, *Magnetostriction: Theory and Application of Magnetoelasticity* (CRC press, Boca Raton, Florida, USA, 1993).
[52] US DOE Public Access Plan, https://www.energy.gov/downloads/doe-public-access-plan.
[53] Y. Ohta and M. Shimizu, J. Phys. F **12**, 1045 (1982).
[54] N. M. Rosengaard and B. Johansson, Phys. Rev. B **55**, 14975 (1997).
[55] P.-W. Ma, C. H. Woo, and S. L. Dudarev, Phys. Rev. B **78**, 024434 (2008).
[56] T. Kaneyoshi, *Introduction to Amorphous Magnets* (World Scientific, Singapore, 1992).
[57] K. Yosida, D. C. Mattis, and K. Yosida, *Theory of Magnetism*, Vol. 122 (Springer-Verlag Berlin, Heidelberg, Germany, 1996).
[58] M. Pajda, J. Kudrnovský, I. Turek, V. Drchal, and P. Bruno, Phys. Rev. B **64**, 174402 (2001).
[59] A. P. Bartók, M. C. Payne, R. Kondor, and G. Csányi, Phys. Rev. Lett. **104**, 136403 (2010).
[60] A. P. Bartók, R. Kondor, and G. Csányi, Phys. Rev. B **87**, 184115 (2013).
[61] M. A. Wood and A. P. Thompson, J. Chem. Phys. **148**, 241721 (2018).
[62] https://github.com/FitSNAP/fitsnap-datasets.git.